

Article

Nanocomposites of Titanium Dioxide and Peripherally Substituted Phthalocyanines for the Photocatalytic Degradation of Sulfamethoxazole

Joanna Musial ^{1,*}, Artium Belet ², Dariusz T. Mlynarczyk ³, Michal Kryjewski ⁴, Tomasz Goslinski ^{3,*}, Stéphanie D. Lambert ², Dirk Poelman ⁵ and Beata J. Stanisz ^{1,*}

- ¹ Chair and Department of Pharmaceutical Chemistry, Faculty of Pharmacy, Poznan University of Medical Sciences, Grunwaldzka 6, 60-780 Poznań, Poland
- ² Department of Chemical Engineering–Nanomaterials, Catalysis, Electrochemistry, University of Liege, Building B6a, Allée du 6 Août 11, B-4000 Liège, Belgium
- ³ Chair and Department of Chemical Technology of Drugs, Faculty of Pharmacy, Poznan University of Medical Sciences, Grunwaldzka 6, 60-780 Poznań, Poland
- ⁴ Chair and Department of Inorganic and Analytical Chemistry, Faculty of Pharmacy, Poznan University of Medical Sciences, Rokietnicka 3, 60-806 Poznań, Poland
- ⁵ LumiLab, Department of Solid State Sciences, Ghent University, Krijgslaan 281 S1, B-9000 Ghent, Belgium
- * Correspondence: joanna.musial@ump.edu.pl (J.M.); tomasz.goslinski@ump.edu.pl (T.G.); bstanisz@ump.edu.pl (B.J.S.)

Citation: Musial, J.; Belet, A.; Mlynarczyk, D.T.; Kryjewski, M.; Goslinski, T.; Lambert, S.D.; Poelman, D.; Stanisz, B.J. Nanocomposites of Titanium Dioxide and Peripherally Substituted Phthalocyanines for the Photocatalytic Degradation of Sulfamethoxazole. *Nanomaterials* **2022**, *12*, 3279. <https://doi.org/10.3390/nano12193279>

Academic Editor: Diana Sannino

Received: 1 September 2022

Accepted: 16 September 2022

Published: 21 September 2022

Publisher's Note: MDPI stays neutral with regard to jurisdictional claims in published maps and institutional affiliations.



Copyright: © 2022 by the authors. Licensee MDPI, Basel, Switzerland. This article is an open access article distributed under the terms and conditions of the Creative Commons Attribution (CC BY) license (<http://creativecommons.org/licenses/by/4.0/>).

Abstract: Phthalocyanines (Pcs) are often used in photosensitization of titanium(IV) oxide, a commonly employed photocatalyst, as such an approach holds the promise of obtaining highly stable and efficient visible light-harvesting materials. Herein, we report on the preparation, characterization and photoactivity of a series of composites based on TiO₂ and peripherally modified metallophthalocyanines: either tetrasulfonated or 4,4',4'',4'''-tetraazaphthalocyanines, with either copper(II), nickel(II) or zinc(II) as the central metal ion. Physicochemical characterization was performed using UV-Vis diffuse reflectance spectroscopy, hydrodynamic particle-size analysis, surface-area analysis using N₂ adsorption-desorption measurements and thermogravimetry combined with differential scanning calorimetry. The band-gap energy values were lower for the composites with peripherally modified phthalocyanines than for the commercial TiO₂ P25 or the unsubstituted zinc(II) phthalocyanine-grafted TiO₂. TG–DSC results confirmed that the chemical deposition, used for the preparation of Pc/TiO₂ composites, is a simple and efficient method for TiO₂ surface modification, as all the Pc load was successfully grafted on TiO₂. The photocatalytic potential of the Pc/TiO₂ materials was assessed in the photocatalytic removal of sulfamethoxazole—a commonly used antibacterial drug of emerging ecological concern. To compare the activity of the materials in different conditions, photodegradation tests were conducted both in water and in an organic medium.

Keywords: photocatalysis; photodegradation; phthalocyanine; sulfamethoxazole; titanium dioxide

1. Introduction

Currently, conventional wastewater treatment facilities do not ensure complete elimination of certain chemical contaminants, including pharmaceuticals, and these are thus termed persistent pollutants. This group of molecules is of particular concern as they are designed to elicit a precise biological response in living organisms [1–5]. More and more often detected in aqueous environments, mostly in sewage, surface water and groundwater, but also in drinking water sources, they may pose a threat to human health and the ecosystem [6,7]. Heterogeneous photocatalysis is an advanced oxidation process (AOP) that has recently emerged as a promising solution to this problem [8,9]. The main idea is

to harvest energy from light to produce strong radicals in water that will chemically degrade the organic pollutants. Titanium(IV) oxide (titanium dioxide, TiO_2) is one of the most commonly used photocatalysts, owing to its good photochemical properties: high photochemical activity, high physical and chemical stability, relatively low cost, simplicity of preparation as well as the possibility of reuse [10,11]. However, technologies based on photocatalysis have not yet been commonly applied on a large scale, mainly due to the narrow light absorption range of the materials. TiO_2 is capable of absorbing light only from the UV region that constitutes merely a few percent of the solar irradiation [12], which limits its activation using natural sunlight. However, these shortcomings can be overcome by various modifications, for instance, grafting the surface of TiO_2 with photoactive compounds [13–16]. One particularly interesting strategy is sensitization with photosensitizers that absorb light in the visible range, as it holds promise of efficient light-harvesting capability.

Organic dyes are the most commonly used photosensitizers for photocatalytic water remediation. A particularly interesting group of such dyes are phthalocyanines (Pcs) – *aza*-porphyrinoids, composed of four isoindole groups linked with *aza*-methine bridges (Figure 1). Many cations may form coordination complexes with phthalocyanines. Depending on the metal ion, the molecular electronic and optical properties can be tailored to some extent [17]. Most importantly, phthalocyanines are photoactive molecules that absorb light in two main wavelength ranges, with peaks around 350 and 670 nm (Soret band and Q band, respectively), and are able to mediate reactive oxygen species (ROS) generation. This favorable absorption spectrum can enable more efficient use of solar irradiation and, therefore, minimize the external energy needed during the application of the AOPs in wastewater treatment (such as the use of a UV lamp). However, most phthalocyanines are non-soluble and prone to aggregation in aqueous solutions [18]. For these reasons, phthalocyanines are effectively used as photosensitizing grafting materials, as both the Pc and the sensitized nanoparticles benefit from such a combination [18–25].

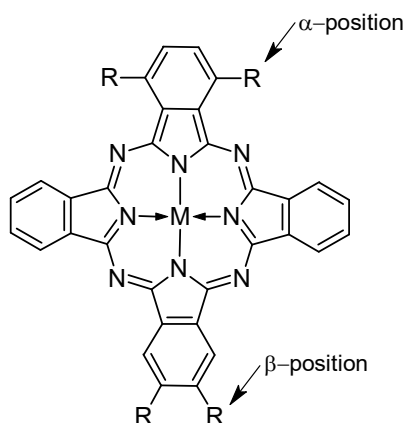


Figure 1. General structure of a phthalocyanine with the non-peripheral (α) and peripheral (β) substitution positions (M = metal cation or 2H).

Encouraged by our earlier results [26,27], we continued the studies on the photocatalytic activity of composites of TiO_2 and phthalocyanines to provide a deeper insight into the structural details of the macrocycles. We tested metallophthalocyanines with different peripheral groups and central metal ions. Peripheral structure modifications can strengthen the attachment of the macrocycle on the surface of TiO_2 by enabling chemical bond formation (instead of physisorption of the photosensitizer on the surface of the photocatalyst). Chemical anchoring is important for two main reasons: it can increase the efficiency of the charge transfer process and also provide good stability of the composites [28]. In addition, the type of metal cation in the phthalocyanine central cavity influences

available TiO₂ P25 (Aeroxide, 21 nm primary particle size, purchased from Sigma-Aldrich). The overview of the procedure is illustrated in Figure 3, and all the modifications are presented in Table 1.

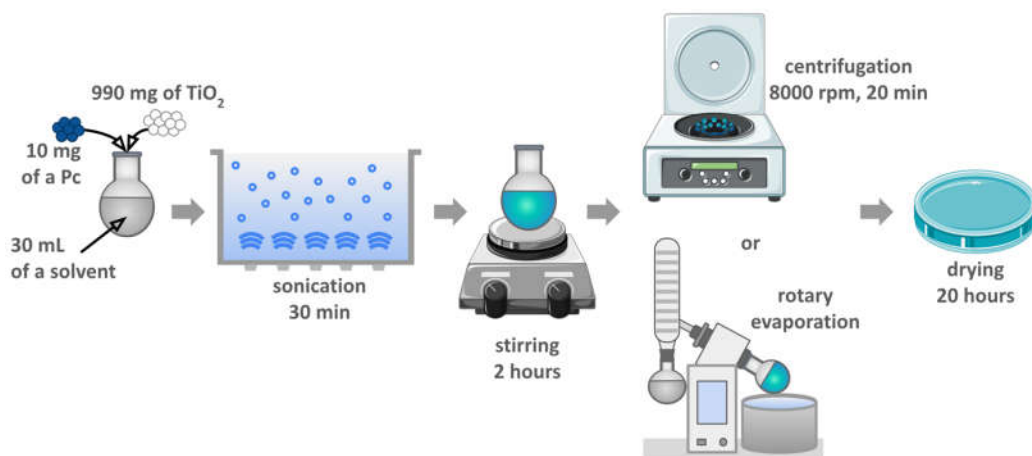


Figure 3. Schematic representation of the preparation of the photocatalytic materials by the chemical deposition method.

Table 1. Modifications to the chemical deposition procedure, specified for each of the prepared materials. n—calculated number of moles of the Pc used.

Pc	Formula	Formula Weight	n [mmol]	Solvent Used	Solvent Removal	pH Adjustment
NiPc_s	Na ₄ C ₃₂ H ₁₂ N ₈ NiO ₁₂ S ₄	979.39	0.010			no
CuPc_p	C ₂₈ H ₁₂ CuN ₁₂	580.02	0.017		centrifuga-	
H ₂ Pc_p	C ₂₈ H ₁₆ CuN ₁₂	520.51	0.019	deionized	tion and	
ZnPc_p	C ₂₈ H ₁₂ N ₁₂ Zn	581.88	0.017	water	washing	yes, to 3–4 ¹
ZnPc_s	Na ₄ C ₃₂ H ₁₂ N ₈ ZnO ₁₂ S ₄	898.18	0.011		with etha-	
CuPc_s	Na ₄ C ₃₂ H ₁₂ CuN ₈ O ₁₂ S ₄	984.25	0.010		nol	
ZnPc	C ₃₂ H ₁₆ N ₈ Zn	577.93	0.017	analytical grade dichloro-	using a ro-	no
				methane	tary evap-	
					orator	

¹ pH was adjusted with HCl and NaOH.

The first step consisted in dissolving 10 mg of the Pc using 30 mL of the solvent (indicated in Table 1) in a round-bottom flask. Next, 990 mg of TiO₂ was added, the suspension was sonicated for 30 min and then stirred for 2 h at room temperature. The solid material was thereafter separated by centrifugation (8000 rpm, 20 min), washed with ethanol, and separated by centrifugation again (8000 rpm, 20 min, repeated three times). In the case of ZnPc deposition, the solvent was removed by using a rotary evaporator. In all cases, the resulting blue solid was dried in air overnight to remove potential residual solvents.

2.3. Characterization of Photocatalytic Materials

2.3.1. UV-Vis Diffuse Reflectance Spectroscopy (DRS)–Band Gap Determination

The band gaps of the photocatalytic materials were determined using diffuse reflectance spectroscopy measurements in the region of 250–800 nm using a Lambda 1050 S UV-Vis-NIR spectrophotometer (Perkin Elmer) equipped with a Spectralon-coated integrating sphere. The recorded diffuse reflectance spectra (R_{sample}) were transformed into absorbance spectra using the Kubelka–Munk equation [33]:

$$F(R_{\infty}) = \frac{(1 - R_{\infty})^2}{2R_{\infty}} \quad (1)$$

where R_{∞} is defined as $R_{\infty} = \frac{R_{\text{sample}}}{R_{\text{reference}}}$ with $R_{\text{reference}}$ being the diffuse reflectance spectrum measured for the Spectralon reference. Spectra were normalized in intensity to 1 by dividing each spectrum by its maximum. Applying the Tauc plot method [34], the following equation:

$$(F(R_{\infty})hv)^{1/m} = C(hv - E_g) \quad (2)$$

(where C is a constant and m is a constant that depends on the optical transition mode), was used to obtain the direct and indirect optical band gap values, $E_{g,\text{direct}}$ (eV) and $E_{g,\text{indirect}}$ (eV), by plotting $(F(R_{\infty})hv)^2$ and $(F(R_{\infty})hv)^{1/2}$, respectively, as a function of the photon energy hv and by determining the intersection of the linear part of the curve and the energy axis.

2.3.2. Hydrodynamic Particle Size

The nanoparticle size distribution in aqueous suspension was evaluated by nanoparticle tracking analysis (NTA) using a *Malvern Panalytical* (Malvern, United Kingdom) *NanoSight LM10* instrument equipped with a sCMOS camera (405 nm laser) and 3.2 Dev Build 3.2.16 software. The nanomaterial dispersions were diluted with deionized water to reach the operating range of nanoparticle concentration. The sample chamber temperature was set and maintained at 25.0 ± 0.1 °C, and the syringe pump infusion rate was set to 200. Three movies of 30 s were recorded for each sample.

2.3.3. Morphological Analysis by the N₂ Adsorption-Desorption Method

A detailed morphological characterization using the N₂ adsorption-desorption method at 77 K was performed using the *ASAP™ 2420 system* (Micromeritics®, Norcross, GA, USA). Prior to the analysis, samples were outgassed at 200 °C for 16 h to remove any undesirable adsorbed species. Information such as specific surface area, external specific surface area, porous volume, porosity, radius and relative average number of contacts (if a spherical geometry is supposed) was retrieved from these analyses.

2.3.4. TG-DSC

Thermogravimetric (TG) analysis coupled with differential scanning calorimetry (DSC) was performed using a *SETARAM® Sensys Evo 3D* TG–DSC with a platinum crucible. Platinum was chosen instead of the commonly used alumina to avoid side reactions as well as diffusion phenomena that could occur when metallic oxides are put together at higher temperatures. Samples of a given mass were heated from room temperature to 800 °C at a rate of 2 °C/min. Grafting yields were calculated from the mass loss. DSC plots provided insights into the chemistry of the Pcs and Pcs immobilized on TiO₂.

2.4. Photochemical Studies

2.4.1. Set-up of the Photocatalytic Experiment in an Organic Solvent

The photodegradation experiments in *N,N*-dimethylformamide (DMF) were carried out in a reactor consisting of a UV-transparent cuvette placed on a magnetic stirrer in the middle and surrounded by three LED lamps, either at 365 (UV) or 665 nm (R). The light intensity was set to 20 mW/cm² and monitored with an *RD 0.2/2* radiometer (Optel) (Figure 4). The cuvette contained a total volume of 3.0 mL, composed of 0.75 mL of SMX solution (20 mg/L), 0.75 mL of a photocatalyst suspension (0.08 mg/mL) and 1.5 mL of DMF. SMX solution was obtained by dilution from a stock solution prepared by dissolving 100 mg of SMX in 5.0 mL of DMF. Similarly, photocatalyst suspensions were obtained by dilution from a stock solution prepared by suspending 6.0 mg of a photocatalytic composite

in 15.0 mL of DMF. Each mixture of SMX and a photocatalyst was irradiated for 10 min while being constantly stirred. The absorbance values at 267 nm, corresponding to the SMX absorption maximum, were measured using a *Jasco V-770 UV-Vis spectrophotometer* (Jasco, Japan) at the following times: 0, 2, 4, 6, 8, and 10 min after starting illumination.

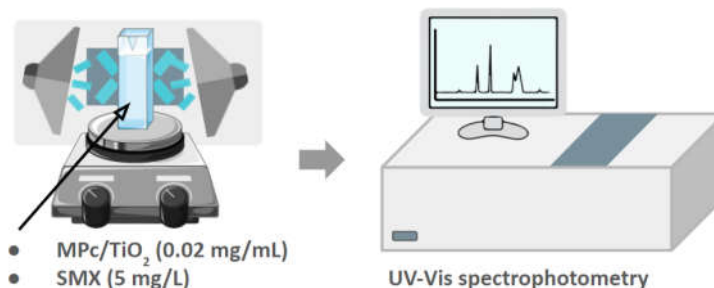


Figure 4. Set-up of the photocatalytic experiment in DMF.

2.4.2. Set-up of the Photocatalytic Experiment in Water

The photodegradation experiments in water were carried out in a reactor consisting of a beaker (transparent for light over 200 nm) placed on a magnetic stirrer and surrounded by three LED lamps, either UV or R, as described before (Figure 5). The beaker contained 200 mL of SMX solution at 20 mg/L. This solution was prepared each time by dilution from a stock solution, prepared beforehand by dissolving 100.0 mg of SMX in 5.0 mL of methanol. Then, 200 mg of photocatalyst was added, and the resulting mixture was sonicated in the dark for 5 min.

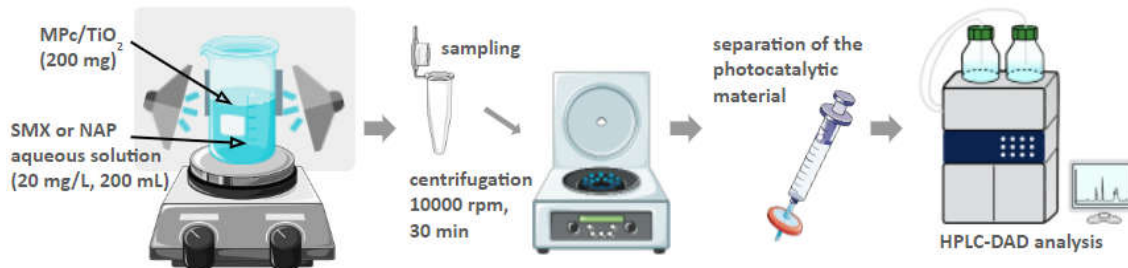


Figure 5. Schematic representation of the set-up and general procedure of the photocatalytic experiment in water.

Next, the mixture was stirred for 30 min without irradiation to reach the adsorption-desorption equilibrium [35–37]. After the ‘dark step’, either UV or R LED lamps were turned on. The mixtures were irradiated for 8 to 24 h while being constantly stirred. Samples of 2 mL were taken in triplicate at the following time points: −0.5, 0, 2, 4, 6, 8, and 24 h. Collected samples were centrifuged at 10,000 rpm for 30 min. Prior to the HPLC analysis, the samples were additionally filtered through 0.2 μm PTFE syringe filters.

SMX concentrations were measured using an HPLC instrument equipped with a diode array detector (DAD) (Agilent 1100 HPLC, USA), operating at a wavelength of 267 nm, and an Agilent Eclipse XDB C18 analytical column (150 × 4.6 mm, 5 μm). The temperature of the column was set at 30 °C. The flow rate was set at 1.0 mL/min, and the injected sample volume was 5 μL. The mobile phase consisted of methanol and water, 50:50 (*v/v*).

3. Results and Discussion

3.1. Preparation of Photocatalytic Materials

TiO₂ P25, a mixture of two polymorphs—anatase and rutile—was chosen as a support for macrocyclic compounds. Rutile is generally considered less active, yet more stable, than pure anatase in photocatalytic applications [38,39]. However, data from several studies show that thanks to a better electron-hole pair separation, the mixed-phase TiO₂ appears to be more active than either pure anatase or pure rutile [40–42]. The nanomaterials were prepared using a simple chemical deposition procedure, yielding a series of photocatalysts, each containing a theoretical 1% (*w/w*) of one of the following phthalocyanines deposited on the surface: **NiPc_s** (NiPc_s/TiO₂), **CuPc_p** (CuPc_p/TiO₂), **2HPc_p** (2HPc_p/TiO₂), **ZnPc_p** (ZnPc_p/TiO₂), **ZnPc_s** (ZnPc_s/TiO₂), **CuPc_s** (CuPc_s/TiO₂), and **ZnPc** (ZnPc/TiO₂) (Figure 6).

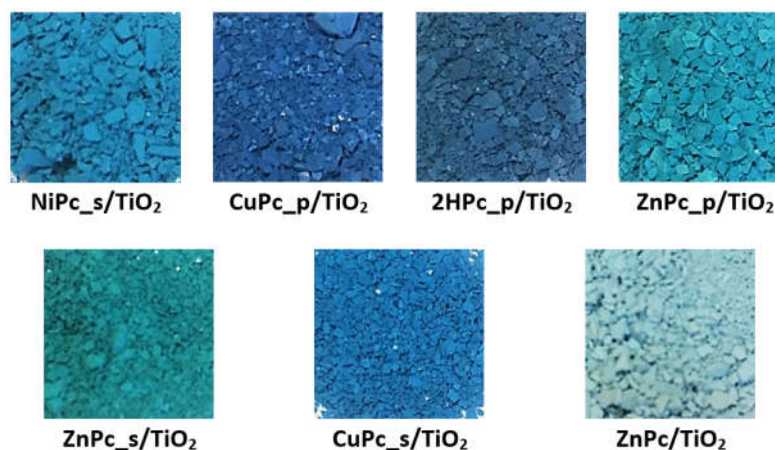


Figure 6. Photographs of the obtained photocatalytic composites.

According to our previous studies, the chemical deposition procedure does not alter the crystallinity of the TiO₂ nanoparticles [26]. During the deposition process, it was noticed that to attach Pcs on the surface of TiO₂ efficiently, the pH of the suspension must be adjusted to 3–4. After centrifugation, which followed 2 h of stirring, it was observed that the solution became colorless and transparent, which indicated that the phthalocyanine was efficiently deposited on the surface of TiO₂. This observation was later confirmed by calculating the Pc content via TG-DSC measurements (Section 3.2.4).

The pH range of 3–4 is below the point of zero charge of TiO₂ [43]. Therefore, a certain amount of positively charged hydroxyl groups on its surface favors the formation of physicochemical bonds with negatively charged, peripheral groups of Pcs. Figure 7 presents possible anchoring modes for both types of peripherally modified Pcs used in the present study. In the case of tetrasulfonated Pcs, in the pH range of 3–4 and considering the pK_a of the sulfonic groups being negative, the main species are all negatively charged sulfonates, and they would form a covalent bond with superficial hydroxyl groups [44–46]. Sulfonic acid groups have been reported to improve the performance of TiO₂-based photocatalysts [47]. The existing literature shows that for sulfonic acid groups, monodentate, bidentate and tridentate binding modes are possible [48–50]. In the case of tetraazaphthalocyanines, a coordination bond between the electron-acceptor sites of titania and the non-shared electron pair of nitrogen in the pyridyl ring can be formed [51–55]. Our observations are in accordance with the work of Mathew et al., who reported that the protonation of each pyridyl nitrogen in 5,10,15,20-tetra(4-pyridyl)porphyrin derivative proceeds step by step, in four equilibrium reactions, with pK_a values estimated to be: 5.3, 4.7, 2.2 and 1.2, respectively [56]. Therefore, in the considered pH range of 3–4, at least two of the four pyridyl nitrogens are protonated. As a consequence, some of the pyridyl rings within the

same Pc are in their basic form, which allows the mechanism shown in Figure 7. Figure S1 shows the distribution of protonated pyridyl species, according to the aforementioned pKa values [57]. Moreover, we observed that acidic conditions were necessary to solubilize the tetraaza-Pc, yet the excess of HCl hampered its deposition on the surface of TiO₂—in such case, after the deposition, the precipitating solid TiO₂ remained white, while the liquid was dark blue. Thus, we can state that a pH of 3–4 provided balanced conditions, favoring both the solubilization of the tetraazaphthalocyanine and the formation of a chemical bond between the pyridyl group and TiO₂.

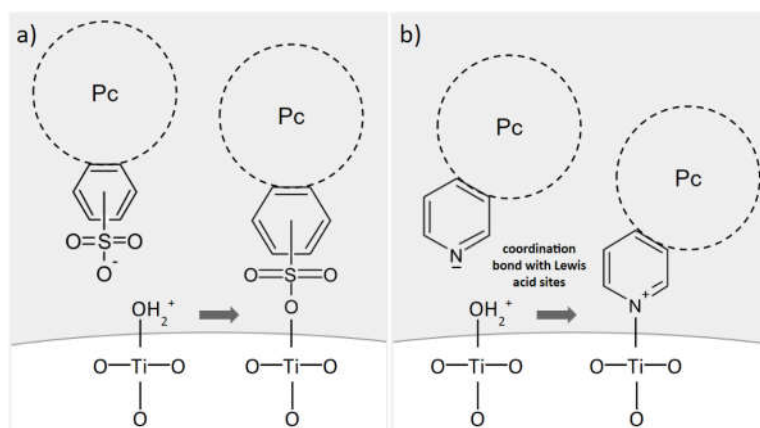


Figure 7. Proposed anchoring modes for (a) sulfonyl and (b) pyridyl peripheral groups of phthalocyanines on TiO₂ surface during the chemical deposition process below the TiO₂ point of zero charge (pH = 3–4). Based on [28,45,53].

Unfortunately, due to the low content of the phthalocyanine (~1%), the formed bond signals could not be directly confirmed by ATR-FTIR analyses, as they overlap with other functional groups in the materials (ester bonds with Ti=O, Ti–OH and H₂O; pyridinium groups with pyridyl groups). The indirect evidence of the chemical bonding between the Pc and TiO₂ surface is that it was impossible to wash out the Pcs with inorganic (both water based HCl or NaOH in case of Pc_p and Pc_s, respectively) or organic (methanol, dichloromethane, *N,N*-dimethylformamide, dimethylsulfoxide, tetrahydrofuran) solvent. After addition of a solvent, the suspension was shaken, sonicated and centrifuged. The resulting supernatants were monitored by UV-Vis, which showed no traces of Pcs.

3.2. Characterisation of Photocatalytic Materials

3.2.1. UV Diffuse Reflectance Spectroscopy (DRS)—Band Gap Determination

The UV-DRS measurements showed that grafting the TiO₂ surface with peripherally-modified Pcs affected the resulting absorption spectra (Figure S2). Compared to bare TiO₂, which absorbs light only in the UV region, the grafted photocatalysts clearly display two regions of absorption: UV and visible (red) region (550–750 nm), corresponding to the Soret and Q bands, respectively. The only exception is the absorption spectrum for ZnPc (without peripheral modifications), which shows strong UV absorption and a relatively weak visible light absorption. Therefore, DRS results transformed into normalized Kubelka–Munk absorption functions confirmed that the obtained materials are capable of absorbing light in the irradiation range of the photocatalytic tests: UV ($\lambda_{\max} = 365$ nm) or R ($\lambda_{\max} = 665$ nm).

Figure 8 presents the comparison of the band-gap energy values (E_g) calculated for each of the photocatalytic materials, assuming the direct as well as the indirect electronic transitions from the valence band to the conducting band (Table S1). Grafting TiO₂ with peripherally-modified phthalocyanines reduced the E_g of the photocatalytic material.

The results are consistent with the literature [58–60]. There is a clear difference between the E_g of bare TiO_2 and the E_g of composites of peripherally-modified Pcs and TiO_2 ; however, these composites express similar E_g values. Interestingly, the E_g for unmodified ZnPc deposited on TiO_2 is equal to that of bare TiO_2 , whereas for other materials containing functionalized derivatives of zinc(II) phthalocyanine, either with peripheral pyridyl (ZnPc_p) or sulfonyl (ZnPc_s) groups, the E_g value is significantly lower.

A graphical representation of the normalized Kubelka–Munk function (Equation (1)) for each photocatalytic material can be found in the Supporting Information (Figures S3 and S4).

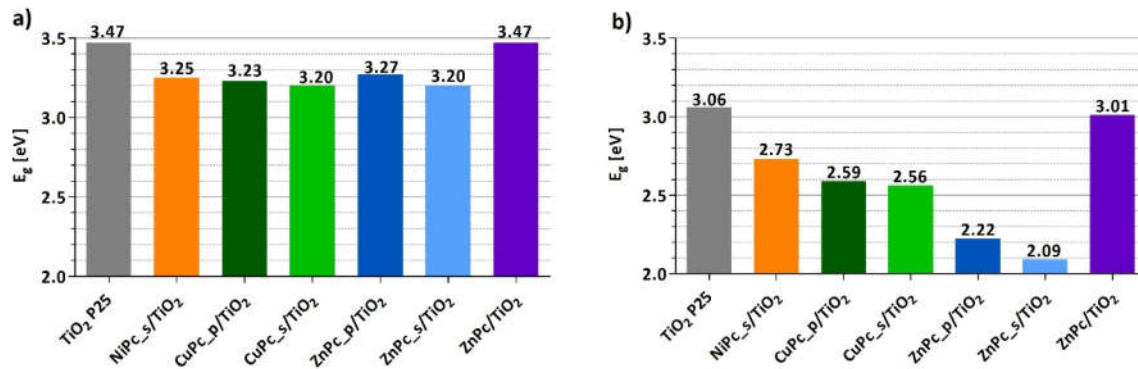


Figure 8. Band-gap energy values (E_g) of each photocatalytic material calculated from DRS measurements using the Kubelka–Munk equation and the Tauc plot method, assuming a direct transition (a) or an indirect transition (b).

3.2.2. Particle Size

The mean hydrodynamic diameter of each composite was determined using nanoparticle tracking analysis. This technique, similar to dynamic light scattering, measures the hydrodynamic diameter of the particles, which is higher than the geometric diameter because it includes the electrical double layer on the particle surface in a liquid medium. The results indicate that each of the tested materials, including unmodified TiO_2 , the particles are prone to agglomeration in a liquid medium (Table 2).

Table 2. Hydrodynamic diameter values of the particles obtained using NTA.

Photocatalytic Material	Mean Hydrodynamic Diameter [nm]	SD [nm]	PDI
TiO_2	240	95	0.16
NiPc_s/ TiO_2	236	105	0.20
CuPc_p/ TiO_2	191	74	0.15
ZnPc_p/ TiO_2	243	182	0.56
ZnPc_s/ TiO_2	216	146	0.46
CuPc_s/ TiO_2	187	74	0.16
ZnPc/ TiO_2	250	98	0.15
TiO_2	240	95	0.16

SD—standard deviation, PDI—polydispersity index, calculated according to the formula $\text{PDI} = (\text{SD}/\text{mean diameter})^2$.

3.2.3. N_2 Sorption Analysis

The specific surface area (S_{BET}) was calculated using the multilayer theory of Brunauer–Emmett–Teller on the adsorption curve of the N_2 sorption experiment at 77 K. The external specific surface (S_{EXT}), as well as the microporous volume, were calculated by the t-plot method (adsorption curve), using the Harkins and Jura statistical thickness

equation extrapolated in the linear range, corresponding to the theoretical formation of a N₂ monolayer. The arbitrary choice of the linearity range affects the calculated values of S_{EXT} and the microporous volume. Although this is still under debate in literature [61], a range between $t = 0.35$ nm and $t = 0.50$ nm was chosen for all materials. The obtained values were found negligible (Table 3), thus all the microporous volumes can be considered approximately 0 cm³/g. The apparent negative values of micropores' volume are the result of the chosen linear range. Further comparison showed no significant differences neither in S_{BET} nor S_{EXT} values among the photocatalytic composites (Table 3). Hence, the obtained results support the assumption that the prepared materials are non-porous.

Table 3. Results of the surface area analysis using the N₂ adsorption-desorption method. S_{BET} is the specific surface area calculated using the multilayer theory of Brunauer–Emmett–Teller and S_{EXT} is the external specific surface calculated by the t-plot method.

Photocatalytic Material	S _{BET} [m ² /g]	S _{EXT} [m ² /g]	t-Plot Micropore Volume [cm ³ /g]	D [nm]
TiO ₂	57	55	0.000178	25.4
NiPc_s/TiO ₂	54	50	0.001488	28.2
CuPc_p/TiO ₂	52	56	−0.002796	25.2
ZnPc_p/TiO ₂	55	54	−0.000191	26.1
ZnPc_s/TiO ₂	52	52	−0.000390	27.3
CuPc_s/TiO ₂	53	53	−0.000993	26.4
ZnPc/TiO ₂	56	58	−0.001720	24.3

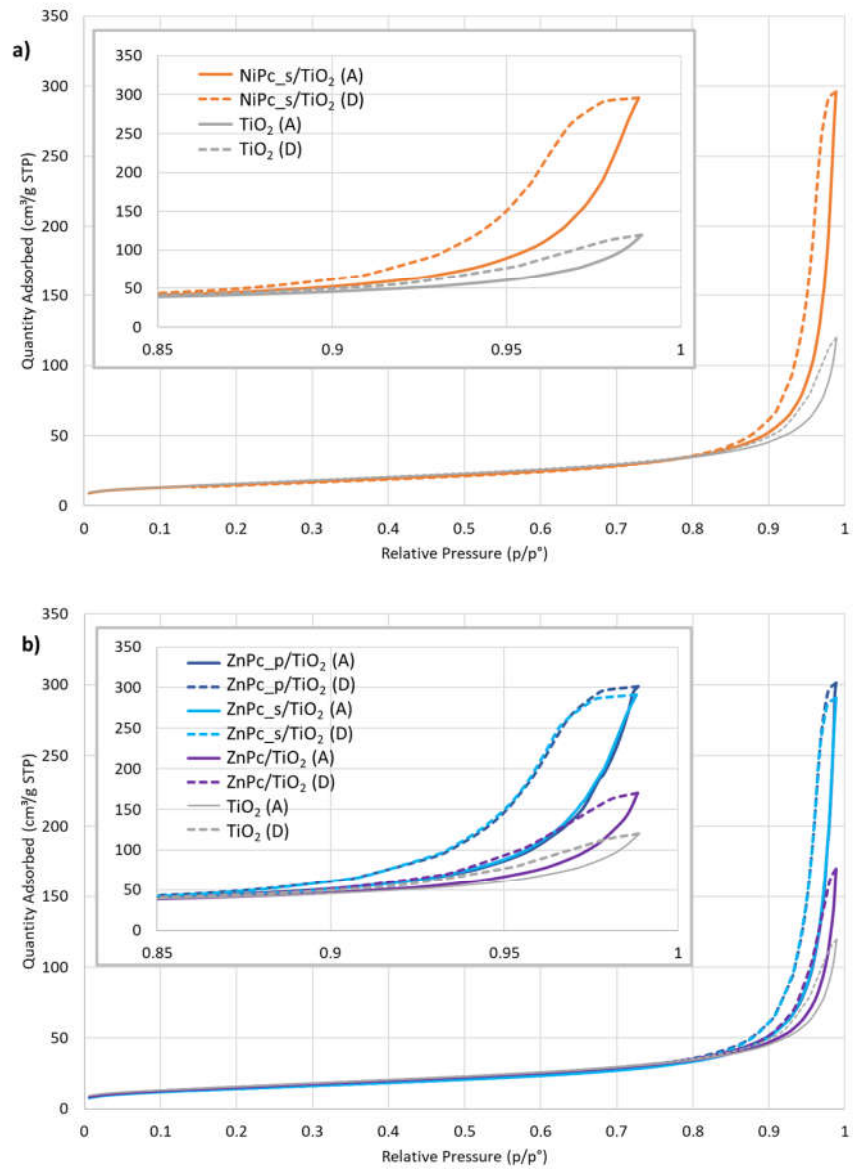
Furthermore, assuming a spherical geometry for the dense non-porous particles, it is possible to calculate a corresponding diameter, or particle size, from S_{EXT} via the following equation:

$$D = \frac{6}{\rho_{\text{TiO}_2} \times S_{\text{EXT}} \times 10^{-3}} \quad (3)$$

where D is expressed in nm, ρ_{TiO_2} is the density of polycrystalline TiO₂ in g/cm³ (a value of 4.26 was considered, as provided by Sigma-Aldrich), and S_{EXT} is in m²/g. The calculated particle sizes are reported in Table 3. For all MPc/TiO₂ materials, we observed a slight increase in the particle size compared to the unmodified TiO₂, in agreement with a system seen as large molecules covering the surface of rigid spheres. Still, a discrepancy is observed between the unmodified TiO₂ particle size calculated here (25.4 nm) and the one provided by Sigma-Aldrich (21 nm). The difference may stem from different characterization techniques used to determine this value or the simplifications used in the provided calculations.

Figure 9 shows N₂ physisorption isotherms for the photocatalytic materials, compared each time with bare TiO₂. According to the IUPAC classification of physisorption isotherms [62], the shape of the isotherms resembles type II and type IV isotherms, the latter type being considered because of the presence of a hysteresis. Hysteresis loops are associated with a capillary condensation phenomenon inside mesopores. However, we stated that our material is non-porous and no sign of mesoporosity has been observed on the t-plot (Figure S5). In accordance with the work of Gommès et al. [63], we understand that mesoporous zones can exist in between rigid spherical particles when the latter agglomerate. Moreover, the authors show that the higher the average number of contacts between spheres (N_c), the higher the amount of N₂ that can be adsorbed (Figure 5 in [63]). The adsorbed amount of N₂ is systematically higher for Pc-grafted TiO₂ particles than for unmodified TiO₂. Similarly, in the case of zinc (II) phthalocyanines, these values are higher for the composites containing peripherally-modified Pc, than for unmodified ZnPc/TiO₂ (Figure 9b). According to Gommès et al., these observations can be qualitatively analysed with the N_c concept, even if without a standard isotherm for a flat non-porous TiO₂, it was impossible to calculate N_c directly. The presence of Pcs at the surface of TiO₂ tends to unambiguously increase N_c, compared to the bare TiO₂: Pcs seem to act as local glue

drops, due to a presumed Van der Waals interaction occurring from both sides of Pcs and joining the two spheres together. Figure 9b shows that this effect is even more pronounced when Pcs are modified with peripheral groups, which can be explained by assuming that among the four peripheral groups, some are attached to one sphere, while the others, initially free, are attached to the other one. Altogether, these analyses corroborate the agglomerates observed during the synthesis and the large distributions obtained from mean hydrodynamic diameter measurements.



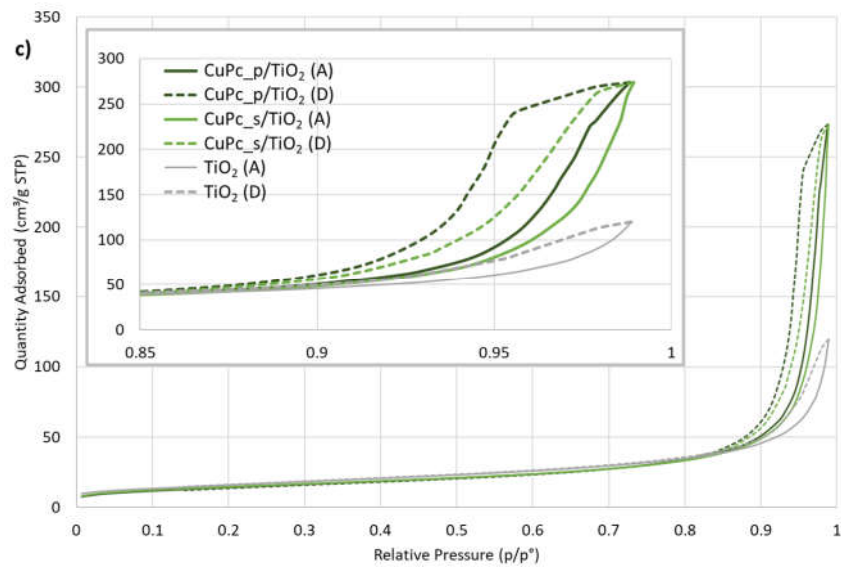


Figure 9. Molecular nitrogen (N_2) physisorption isotherms at 77 K for: (a) NiPc_s/TiO₂, (b) ZnPc_s/TiO₂, ZnPc_p/TiO₂ and ZnPc/TiO₂, (c) CuPc_p/TiO₂ and CuPc_s/TiO₂; A—adsorption isotherm, D—desorption isotherm.

3.2.4. TG-DSC

The thermal stability of the materials and the amount of phthalocyanine deposited on the surface of TiO₂ were analyzed by using TG-DSC. As shown in Figure 10, all the nanocomposites display quite similar behavior during heating. A slight mass loss, which occurs up to 150 °C is attributed to water evaporation, while the mass loss of interest occurs between 200 °C and 450 °C. The mass loss values and the corresponding temperature ranges for each nanocomposite are summarized in Table 4. For further details about our considerations for temperature values, please refer to the Supporting Information, where first derivatives of TG signals guided our choices (Figure S6). The obtained results confirmed the close theoretical 1% (*w/w*) Pc content in each photocatalytic material. This proves that during the chemical deposition process, all the weighed Pc was successfully grafted on the surface of TiO₂. In the case of bare TiO₂, 1.9% of mass loss is observed, which at first seems high, compared to the Pc-grafted TiO₂ materials (Figure 10) [64–66]. However, a closer look at the mass loss up to 150 °C suggests that bare TiO₂ can adsorb more water than Pc-grafted TiO₂ due to its high surface hydrophilicity. This explains why, in some cases in Figure 10, the bare TiO₂ TG curve goes below the Pc-grafted material one, even though one expects the former being above the latter. Therefore, we conclude that the hydrophilicity of the Pc-grafted materials is lower because of the lesser availability of hydrophilic sites on the surface; those sites are mainly surficial titanol groups, as well as superficial oxygen atoms from a metalloxane (Ti–O–Ti) group. The only exception seems to be NiPc_s/TiO₂, which is able to adsorb the same amount of water as bare TiO₂. One way to explain this observation is that Pcs, with their planar structure, cover the surface of the particle (Van der Waals interactions), instead of being loosely attached by one ending group, which results in a decrease of available hydrophilic sites.

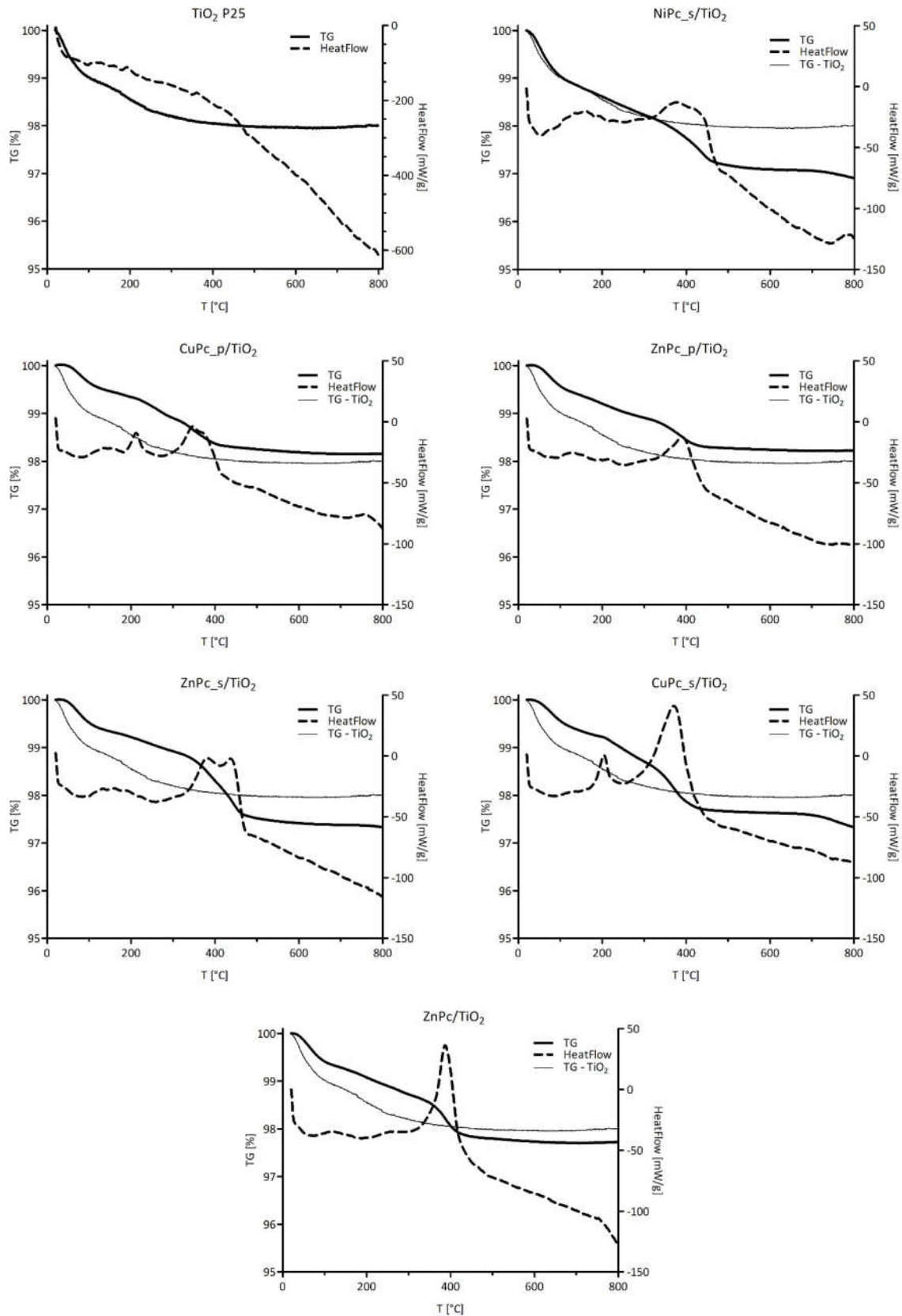
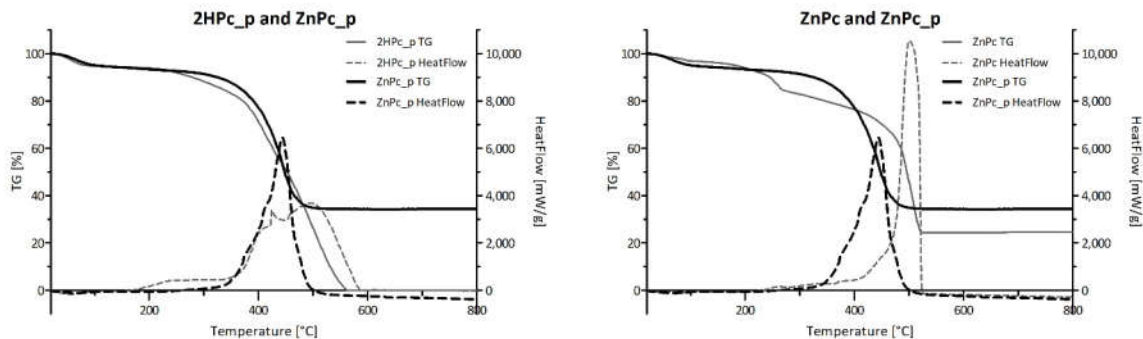


Figure 10. TG–DSC of prepared photocatalytic composites: TG and HeatFlow data.

Table 4. Results of the TG-DSC analysis for each photocatalytic composite. The mass loss temperature ranges were determined based on the data shown in Figure S6.

Photocatalytic Material	Temperature Range [°C] of the Mass Loss		Mass Loss [%]	Sample Mass [mg]	Mass Loss [mg]
	Onset	Offset			
TiO ₂	20	340	1.9	10.3	0.19
NiPc_s/TiO ₂	302	467	1.0	40.1	0.40
CuPc_p/TiO ₂	200	306	1.0	59.2	0.59
	306	450			
ZnPc_p/TiO ₂	167	255	0.9	48.5	0.44
	305	460			
ZnPc_s/TiO ₂	301	480	1.3	50.9	0.66
CuPc_s/TiO ₂	199	239	1.2	60.6	0.73
	305	443			
ZnPc/TiO ₂	309	458	0.9	38.8	0.35

Figure 11 presents the comparison of TG-DSC results conducted for four neat phthalocyanines: 2HPc_p, ZnPc_p, ZnPc_s and ZnPc. Contrary to zinc(II) phthalocyanines, 2HPc_p was completely decomposed due to its purely organic structure. In the case of each of the three tested zinc(II) phthalocyanines, regardless of its peripheral group, the final mass loss was equal to 66%, 65% and 75% for ZnPc_p, ZnPc_s and ZnPc, respectively. These results are consistent with the literature and indicate that zinc compounds, which do not undergo further degradation in the tested temperature range, are formed [67,68]. Interestingly, when ZnPc and ZnPc_p are compared, a shift of the HeatFlow peak towards lower temperature can be observed. As the heat needed for the combustion of both Pcs is the same (Table 5), we can state that the shift is a result of the presence of nitrogen atoms in the pyridyl ring, which most certainly imposes a different reaction pathway than during the combustion of the unsubstituted ZnPc. In contrast, the graphical comparison between ZnPc and ZnPc_s, as well as data in Table 5 show that the heat needed for the combustion of the ZnPc_s is lower than for ZnPc ($Q_{\Delta m} = 9778.00$ J/g and 13,100 J/g for ZnPc_s and ZnPc, respectively). This finding is rather unexpected, as the addition of peripheral groups to the macrocyclic structure should require more energy input throughout the combustion process. However, it is possible that the oxygen atoms in sulfonic groups facilitate the process, reducing the heat needed for combustion.



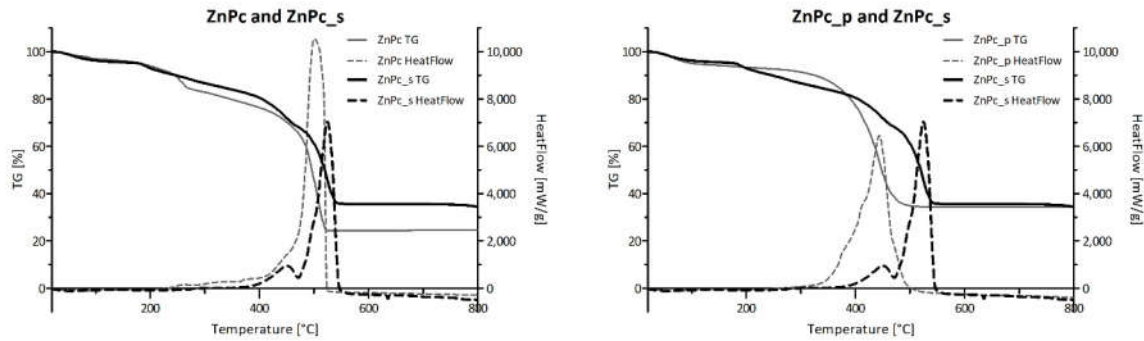


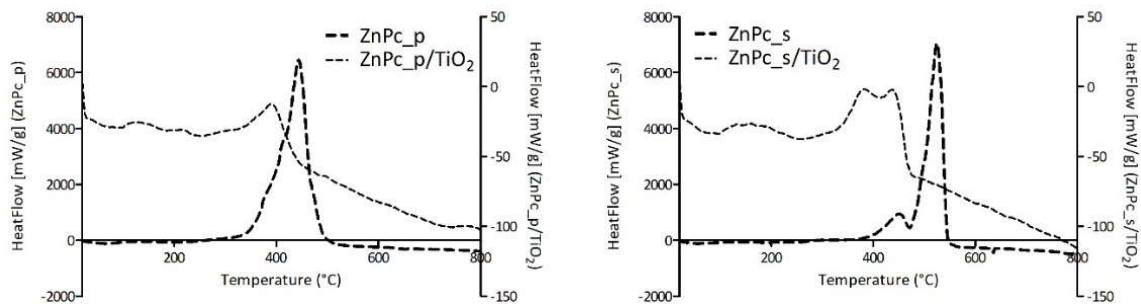
Figure 11. Comparison of the TG and HeatFlow curves between neat phthalocyanines.

Table 5. Comparison of the heat values needed for the combustion of the neat phthalocyanines (ZnPc_p, ZnPc_s, ZnPc) and in the photocatalytic composite with TiO₂ (ZnPc_p/TiO₂, ZnPc_s/TiO₂, ZnPc/TiO₂).

Photocatalytic Material	m _s [mg]	Q [J/g]	Q • m _s [J]	Δm [mg]	Q _{Δm} [J/g]
ZnPc_p/TiO ₂	48.5	112.33	5.45	0.54	10,033
ZnPc_p	13.0	-	-	-	13,000
ZnPc_s/TiO ₂	50.9	189.19	9.64	0.78	12,349
ZnPc_s	13.8	-	-	-	9778
ZnPc/TiO ₂	38.8	214.05	8.31	0.51	16,285
ZnPc	15.9	-	-	-	13,000

m_s—mass of the sample, Q—heat corresponding to the combustion of the Pc content deposited on TiO₂ (calculated per gram of the photocatalytic composite), Δm—mass change in the temperature range corresponding to the combustion of the Pc, Q_{Δm}— heat needed for the combustion of the Pc (calculated per gram of the Pc).

Furthermore, HeatFlow values obtained for each photocatalytic composite of TiO₂ and zinc(II) phthalocyanine derivative and the corresponding neat Pc were set together in Figure 12. A shift of the HeatFlow peak for the neat Pc to higher temperatures can be observed when compared with the HeatFlow peak for Pc/TiO₂ composites. This results from the adsorption of the Pc on TiO₂, wherein the Pc on the surface of the material is more prone to combustion. It is generally acknowledged that combustion reactions occur via mechanisms involving, among others, hydroxyl radicals. We can assume that the proximity of Pcs to superficial hydroxyl groups of TiO₂ facilitates the oxidation reactions. Hence, the shift to lower temperatures is understandable since lower thermal energy is required for those radicals to be formed from titanol groups than from oxygen species.



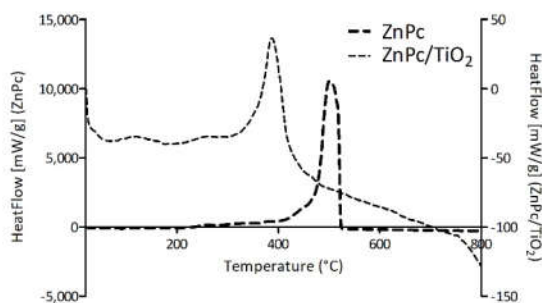


Figure 12. Comparison of the HeatFlow curves for neat phthalocyanines and phthalocyanine-grafted TiO₂.

Moreover, the heat needed for the combustion of the phthalocyanine content in the photocatalytic composite was calculated and compared with the values obtained for the neat phthalocyanine. The results presented in Table 5 show that the heat values needed for the combustion of the Pc deposited on TiO₂ nanoparticles are in the same order of magnitude as the values obtained for the neat Pc.

3.3. Photochemical Studies

The photocatalytic potential of the Pc-TiO₂ nanocomposites was further assessed in drug degradation experiments. Sulfamethoxazole, a bacteriostatic sulfonamide compound, was chosen for the photodegradation tests as a benchmark contaminant often detected in wastewater effluents. Moreover, its elimination from the environment is of particular importance, as the dissemination of antimicrobials contributes to the progression of antibiotic microbial resistance [69–71].

The photocatalytic experiments were conducted in two different media—*N,N*-dimethylformamide and water—as the environment of the photocatalytic reaction is known to influence the type of the produced ROS and the aggregation tendency of metalloporphyrinoids [17]. In general, the interaction between the excited photocatalyst and oxygen may occur via type I or type II reactions. As a result of type I reactions, consisting in electron transfer, hydroxyl radicals ($\cdot\text{OH}$), hydrogen peroxide (H_2O_2) and superoxide anion ($-\text{O}\cdot_2$) are produced. Type II reactions generate singlet oxygen ($^1\text{O}_2$), which has a very short lifetime in water [72]. Therefore, comparing the efficiencies of the photocatalysts in two different solvents was necessary to describe photochemical mechanisms that may drive the degradation process. Other factors that may affect the photodegradation performance include the linkage mode between the photosensitizer and the photocatalyst, the metal ion coordinated to the photosensitizer and the wavelength of light used for activation [14]. Therefore, for a clear comparison between TiO₂ nanoparticles grafted with different phthalocyanines, distilled water was used to limit the number of variables that might have an additional impact on the photocatalytic process. The temperature of the mixture during the experiment did not exceed 30 °C. It should be noted that due to the analytical conditions (such as the need to use UV-Vis spectrophotometry to quickly analyze the samples, which required dilution of the photocatalyst suspension, as well as the adjustment of the absorbance values), the photocatalyst-to-SMX ratio in the photodegradation experiments in DMF was different than in the tests in water. The experiments, either in DMF or water, were carried out separately under the UV- (365 nm) or red- (665 nm) light irradiation to test which component of the composite takes part in the process or whether the SMX decomposition is a result of the charge transfer between the two moieties.

3.3.1. Photocatalytic Degradation of Sulfamethoxazole in Organic Solvent

During the SMX photodegradation experiments in *N,N*-dimethylformamide under UV light (Figure 13a), two composites, namely NiPc_s/TiO₂ and CuPc_s/TiO₂, turned out to be the most effective, leading to 25 and 21% of SMX removal within 10 min, respectively. These two materials displayed higher activity than other Pc-grafted TiO₂ nanoparticles obtained. A slight reduction in SMX content can also be noticed for CuPc_p/TiO₂. Surprisingly, the use of both zinc(II) Pcs, modified with either sulfonyl or pyridyl groups, showed no significant changes in SMX concentration. Unmodified TiO₂ also displayed no activity due to the low concentration and quenching of hydroxyl radicals in DMF [73]. We suppose that the photocatalytic mechanism occurs via type II reaction, namely energy transfer mechanism, involving the formation of singlet oxygen and organic radicals [17,74].

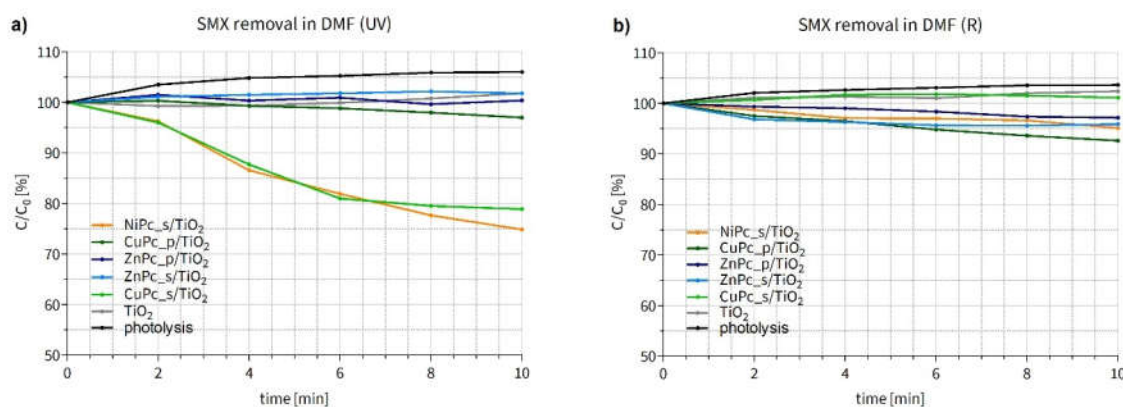


Figure 13. Changes in sulfamethoxazole concentration after (a) UV irradiation (365 nm light) (b) after R irradiation (665 nm light) of the DMF suspension containing a photocatalyst. The trend observed for SMX photolysis is the result of dynamic interactions between SMX molecules and DMF under irradiation conditions. Over the experiment time, SMX molecules formed associates with DMF (the absorbance values in UV-Vis measurements increased and reached plateau).

During the experiment conducted under red irradiation (Figure 13b), a slight reduction of the SMX concentration was observed in the experiments conducted under R light with CuPc_p/TiO₂, ZnPc_s/TiO₂, ZnPc_p/TiO₂ and NiPc_s/TiO₂. Nevertheless, none of the materials was distinctively more active than the others. As mentioned before, bare titanium dioxide is generally not expected to be activated with visible light and to enable decomposition of the target substance in DMF. Interestingly, the effectiveness of CuPc_p/TiO₂ was even slightly higher under R than UV irradiation. Moreover, in contrast to the results shown in Figure 13a, CuPc_s/TiO₂ displayed no visible activity in the red light.

To correctly compare the results obtained in both experiments, a few aspects should be taken into account. First, the light power was equal in all experiments (20 mW/cm²). Although, the number of photons was higher in the case of R irradiation ($6.69 \times 10^{20} \text{ m}^{-2}\text{s}^{-1}$) than UV irradiation ($3.67 \times 10^{20} \text{ m}^{-2}\text{s}^{-1}$), the photon energy of red light ($5.45 \times 10^{-19} \text{ J}$) is lower compared to the ultraviolet wavelength ranges ($2.99 \times 10^{-19} \text{ J}$). Second, UV light is absorbed by both parts of the composite, TiO₂ and the phthalocyanine (in the Soret band), while red light—only by the Pc (in the Q band). Third, the photocatalyst-to-SMX ratio was low (4:1), and the phthalocyanine content constituted 1% (*w/w*) of each composite. Taking all of this into account, the slight, but progressing, reduction of the SMX content during the experiment under red irradiation, especially using CuPc_p/TiO₂, can be considered a promising result. To facilitate the quantitative comparison of the degradation rates mediated by the photocatalysts, reaction constants of the studied processes were calculated for the best two materials (Table 6).

Table 6. The SMX degradation reaction rate constants (first-order reaction model) under UV irradiation with Pc-grafted TiO₂ composites in DMF.

Photocatalytic Material	k [s ⁻¹]	R
NiPc_s/TiO ₂	5.13×10^{-4}	0.996
CuPc_s/TiO ₂	4.60×10^{-4}	0.988

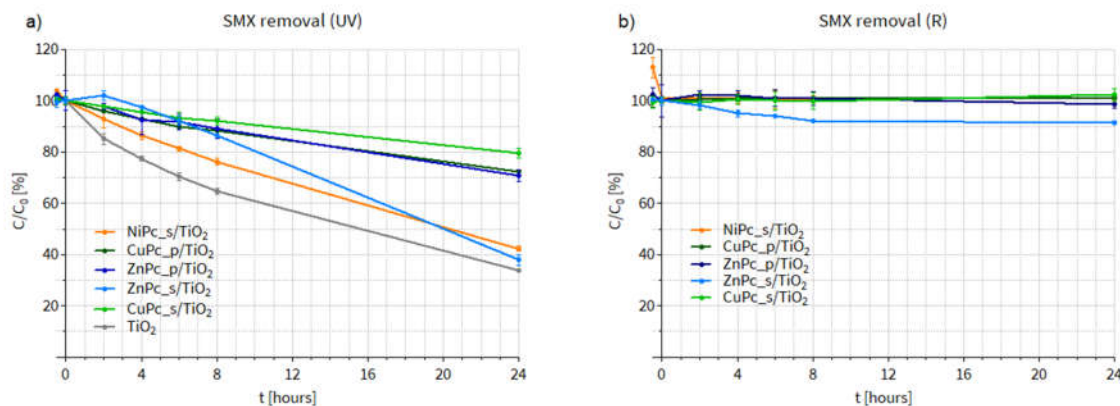
Furthermore, to better compare the performance of our photocatalytic materials in the SMX photodegradation tests under UV irradiation, we have normalized the results of the experiment by the molar quantity of deposited Pc. In fact, as the Pc content in each composite is 1% (*w/w*), and there are considerable differences between the molar mass values of the Pcs, the photodegradation results can be reconsidered. ΔC normalized values presented in Table 7 confirm NiPc_s/TiO₂ and CuPc_s/TiO₂ being the most efficient photocatalysts in SMX degradation and show that NiPc_s/TiO₂ is, in fact, 44% better than CuPc_s/TiO₂, even though in Figure 13a NiPc_s/TiO₂ and CuPc_s/TiO₂ seem to have similar effectiveness. All the calculations are available in the Supporting Information (Table S3).

Table 7. ΔC normalized values, calculated from relative SMX concentrations during the degradation experiment in DMF.

	NiPc_s/TiO ₂	CuPc_p/TiO ₂	ZnPc_p/TiO ₂	ZnPc_s/TiO ₂	CuPc_s/TiO ₂
ΔC , normalized	2.24	0.17	-0.03	-0.11	1.56

3.3.2. Photocatalytic Degradation of Sulfamethoxazole in Water

Having assessed the activity of our photocatalysts in DMF, we conducted SMX photodegradation tests in water (Figure 14). In this case, the SMX removal process occurred more slowly. Under UV irradiation (Figure 14a), NiPc_s/TiO₂ was again the most active material among all the Pc-grafted TiO₂ composites. Nevertheless, none of the materials was more efficient than the bare TiO₂. It should be added that during the experiment under UV light conducted using ZnPc_s/TiO₂, discoloration of the photocatalytic mixture was observed, which proves that a photobleaching effect occurred. This phenomenon consists in the degradation of the organic dye due to the attack of ¹O₂ on the macrocyclic ring. Alternatively, the discoloration might be a result of ZnPc_s deposited on the surface of TiO₂ being more susceptible to the attack of hydroxyl radicals than SMX or alternatively of easier access of ROS to the anchored Pc than to SMX in solution. Therefore, the final efficiency of ZnPc_s/TiO₂ in SMX removal under UV light was similar to that of the bare TiO₂, because after the photobleaching occurred and the Pc was degraded, TiO₂ was exposed to the UV light.

**Figure 14.** Changes in sulfamethoxazole concentration after (a) UV irradiation (365 nm light) (b) after R irradiation (665 nm light) of the water suspension containing a photocatalyst.

Noteworthy, when comparing the SMX degradation results available in the literature, several factors should be taken into account, for example, the power of the irradiation source. Nowadays, most lab-scale experiments are conducted using high-power lamps, which allow researchers to obtain high removal efficiencies. However, these conditions are difficult (and uneconomic) to implement on a large scale. In the present study, low-power LED lamps were used and, consequently, lower, yet more realistic, degradation rates were noted.

During the experiment under R irradiation, shown in Figure 14b, no changes in SMX concentration were observed when other materials (NiPc_s/TiO₂, ZnPc_p/TiO₂, CuPc_s/TiO₂, CuPc_p/TiO₂) were used. Only the use of ZnPc_s/TiO₂ led to 10% SMX removal. In this case, the discoloration of the photocatalytic suspension was less distinct, probably due to the lower energy of the red irradiation, compared to UV light. However, Zn(II) Pcs generally display moderate to high ¹O₂ quantum yields (in DMF, DMSO, water and methanol) [17], so the fact that the 10% SMX removal occurred within the first 8 h of the experiment and the curve for ZnPc_s/TiO₂ reached a plateau may be a sign of the Pc degradation.

Having this in mind, the results from the experiment in DMF, presented in the previous section, should be reconsidered. Figure 13b shows a similar trend for the ZnPc_s/TiO₂: first, relatively rapid SMX degradation (0–6 min), followed by almost no changes in the drug concentration for the next 4 min until the end of the experiment. In the case of the photocatalytic tests in DMF, due to the low photocatalyst-to-SMX ratio, the discoloration of the suspension was practically impossible to notice. Therefore, we suppose that the photobleaching effect in the case of ZnPc_s/TiO₂ might have also taken place during the experiments in DMF under UV-irradiation. It seems possible that this material displayed high activity, which resulted in the degradation of the dye instead of SMX. The calculated rate constants for the SMX degradation in water under UV light are presented in Table 8.

Table 8. The SMX degradation reaction rate constants (first-order reaction model) under UV irradiation with Pc-grafted TiO₂ composites in water.

Photocatalytic Material	k [s ⁻¹]	R
TiO ₂	1.32 × 10 ⁻⁵	0.998
NiPc_s/TiO ₂	9.89 × 10 ⁻⁶	0.999
ZnPc_p/TiO ₂	4.03 × 10 ⁻⁶	0.994

The regression parameters for ZnPc_s/TiO₂ were not calculated due to the observed photobleaching effect during the experiment.

Similar to the previous section, the SMX concentration values measured throughout the experiment under UV irradiation in water were also normalized to better compare the influence of the Pcs deposited on TiO₂. However, in this case, the results obtained in the SMX degradation experiment are normalized by the available surface area of TiO₂ (not occupied by the Pc content). As shown in Figure 14a, none of the Pc-grafted materials turned out to be more active than the bare TiO₂. Therefore, the following hypothesis can be put forward: if a Pc covers with TiO₂ its entire surface, it occupies a certain part of the titania's active surface area, blocking the incident UV light and hampering photoexcitation. Taking into account the actual Pc content on TiO₂, obtained thanks to the TG-DSC analyses, and the TiO₂ surface area calculated using the t-plot results, the % coverage of the photocatalyst surface was calculated, and the remaining available surface was used to normalize the results. The obtained values are presented in Figure 15. It is apparent that NiPc_s/TiO₂ stands out as the best material (apart from ZnPc_s/TiO₂, which underwent photobleaching). Interestingly, the SMX degradation curve for this material lies below the curve for the bare TiO₂, which indicates that the presence of NiPc_s is favorable for the photocatalytic reaction, given the same photocatalytically active surface area. All the calculated values are available in the Supporting Information (Table S4).

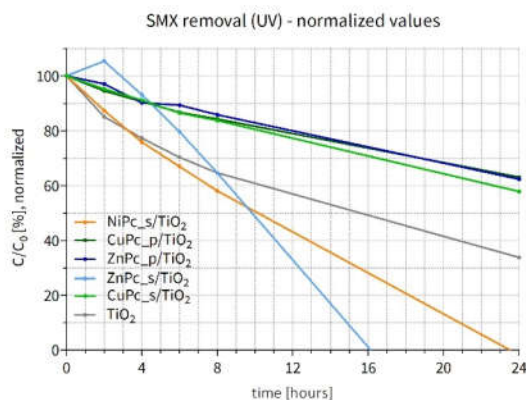


Figure 15. Changes in sulfamethoxazole concentration after UV irradiation (365 nm light) of the water suspension containing a photocatalyst—normalized results.

In this project, the photocatalytic composites were used in bulk form, suspended in the reaction mixture. After the experiments, they were easily removed by centrifugation and filtration, as they tend to form agglomerates in a liquid medium. Although using bulk materials allows for reaching higher reaction rates, thanks to a larger photocatalytically active surface available [75], on an industrial scale, it would require additional separation techniques to remove the photocatalysts from a slurry reactor. To avoid this problem, the photocatalysts could be immobilized, for example, incorporated into a film [9]. Such an approach allows us to eliminate leaching and, consequently, the safety concerns towards TiO₂ applied in photocatalytic processes [76].

The present study focused on describing the relationship between the physicochemical properties and the activity of the Pc-TiO₂ photocatalytic composites. However, to successfully implement these materials in the industrial-environmental practice, further studies should confirm their long-time stability, ex. in cycle testing. Nevertheless, in the case of the most active composites, such as ZnPc_s/TiO₂, longer irradiation led to the photo-bleaching of the phthalocyanine. This phenomenon was associated with the lack of energy transfer from Pcs to TiO₂, which could result in the production of singlet oxygen by Pcs. Singlet oxygen is a ROS characterized by a short half-life, especially in water. This suggests it would react with the Pc and not reach SMX molecules (alternatively, the phthalocyanine blocking the access of SMX to TiO₂ would be exposed to the hydroxyl radicals produced by TiO₂, which in turn would cause its degradation instead of SMX).

Although the presented Pc-TiO₂ composites materials absorb visible light, they did not show any photoactivity in the red light region. Nevertheless, further attempts to improve their photocatalytic activity, such as testing under irradiation of other wavelength region or applying another preparation procedure, could be an interesting continuation of the present study.

4. Conclusions

Herein, new photocatalytic composites of TiO₂ and peripherally modified phthalocyanines were fabricated by chemical deposition. The presented preparation procedure is simple and efficient, as it does not require multiple steps or high energy consumption and allows for complete deposition of the phthalocyanine on the titania surface. The materials were characterized using UV-diffuse reflectance spectroscopy, hydrodynamic particle-size analysis (*NanoSight*), surface-area analysis (N₂ adsorption-desorption method) and thermogravimetry with differential scanning calorimetry. The UV-DRS measurements showed that the peripheral modification of the macrocyclic compounds deposited on TiO₂ results in lower band-gap energy values (calculated for direct and indirect transition modes) than bare TiO₂ or unmodified zinc(II) phthalocyanine-TiO₂ composite. Particle-

size analysis demonstrated that in water, the composites tend to agglomerate, as their hydrodynamic diameter is much higher than the geometric diameter of the commercial nanosized TiO₂ P25. Surface-area analysis using the nitrogen adsorption-desorption method indicated that although the tested materials are non-porous, mesopores are formed between the particles in agglomerates. The hysteresis loops, associated with capillary condensation in mesopores, indicated that for the composites containing peripherally-modified Pc, there were more contact points between the particles in agglomerates when compared to unmodified ZnPc/TiO₂ and bare TiO₂.

Furthermore, the Pc/TiO₂ composites were applied in the photocatalytic degradation of sulfamethoxazole (SMX), an antibacterial drug. During the SMX removal experiments in an organic medium under UV irradiation, two composites were significantly more effective than the neat TiO₂: NiPc_s/TiO₂ and CuPc_s/TiO₂. Under visible irradiation in the red region of the spectrum four materials led to higher SMX photodecomposition CuPc_p/TiO₂, NiPc_s/TiO₂, ZnPc_s/TiO₂ and ZnPc_p/TiO₂. The SMX photocatalytic degradation tests in water showed that only one composite, namely NiPc_s/TiO₂, led to comparable SMX removal as the bare TiO₂.

The physicochemical characteristics of phthalocyanine-modified TiO₂ nanoparticles collected in this paper prove that photosensitization with organic dyes is a promising strategy to obtain a highly active and stable photocatalyst. Nevertheless, implementation of the described materials requires further efforts to enhance the performance of the composites in photocatalytic degradation of emerging contaminants.

Supplementary Materials: The following supporting information can be downloaded at: www.mdpi.com/2079-4991/12/19/3279/s1, Scheme S1: Synthesis scheme of 4,4',4''-tetraaza-29H,31H-phthalocyanine; Scheme S2: Synthesis scheme of zinc(II) 4,4',4''-tetraaza-29H,31H-phthalocyanine; Scheme S3: Synthesis scheme of zinc(II) phthalocyanine-tetrasulfonic acid; tabe S1: Distribution of HiPyr species; Figure S2: Normalized Kubelka–Munk function for the tested photocatalysts; Figure S3. Band gap determination for the prepared nanomaterials—direct transition; Figure S4: Band gap determination for the prepared nanomaterials—indirect transition; Table S1: Trend line equation, correlation coefficient (R) and band gap energy values of each photocatalytic material calculated from DRS measurements using the Kubelka–Munk equation and the Tauc plot method: a) direct transition, b) indirect transition; Figure S5: t-plots determined using Harkins and Jura statistical thickness equation on the adsorption curve (N₂ at 77 K); Figure S6: TG-DSC of prepared photocatalytic composites of phthalocyanines and TiO₂ nanoparticles (TG and dTG data); Figure S8: TG-DSC of neat phthalocyanines (TG and dTG data); Table S2: Percentage coverage determination from TG-DSC and N₂ adsorption.; Figure S9: Comparison of SMX degradation rate constants (k, s⁻¹) under UV irradiation with different photocatalysts; Table S3: Relative concentrations of SMX during the degradation experiment in DMF and ΔC normalized values; Figure S10: Comparison of SMX degradation rate constants (k, s⁻¹) under UV irradiation with different photocatalysts; Table S4: SMX photodegradation values normalized by the TiO₂ surface available (100% considered available for neat TiO₂).

Author Contributions: Conceptualization: J.M., D.T.M. and B.J.S.; methodology: J.M., A.B., D.T.M. and M.K.; validation: J.M., M.K. and B.J.S.; formal analysis: J.M., A.B., D.T.M., T.G., S.D.L., D.P. and B.J.S.; investigation: J.M., A.B. and D.T.M.; resources: T.G., S.D.L., D.P. and B.J.S.; data curation: J.M., A.B., M.K., S.D.L., D.P. and B.J.S.; writing—original draft preparation: J.M., A.B. and D.T.M.; writing—review and editing: M.K., T.G., S.D.L., D.P. and B.J.S.; visualization: J.M., A.B. and D.T.M.; supervision: T.G., S.D.L., D.P. and B.J.S.; project administration: T.G.; funding acquisition: T.G. All authors have read and agreed to the published version of the manuscript.

Funding: This research was funded by the National Science Centre, Poland, grant number 2016/21/B/NZ9/00783.

Data Availability Statement: All the data obtained in this study is presented either in the manuscript or in the Supplementary Materials.

Acknowledgments: The authors would like to thank Aleksandra Gałach for her help with the experiments, and Christelle Alié and Julien Mahy for fruitful discussions. S. D. Lambert thanks the “Fonds National de la Recherche Scientifique–FNRS” for her Senior Research Associate position.

Naproxen was a generous gift from Agnieszka Zgoła-Grześkowiak (Faculty of Chemical Technology, Poznan University of Technology). Zinc(II) phthalocyanine was a generous gift from Wojciech Szczołko (Chair and Department of Chemical Technology of Drugs, Poznan University of Medical Sciences). Images and icons: Servier Medical Art (smart.servier.com), DataBase Center for Life Science (DBCLS; <https://doi.org/10.7875/togopic.2020.145>).

Conflicts of Interest: The authors declare no conflict of interest. The funders had no role in the design of the study; in the collection, analyses, or interpretation of data; in the writing of the manuscript; or in the decision to publish the results.

References

1. Burns, E.E.; Carter, L.J.; Kolpin, D.W.; Thomas-Oates, J.; Boxall, A.B.A. Temporal and Spatial Variation in Pharmaceutical Concentrations in an Urban River System. *Water Res.* **2018**, *137*, 72–85, doi:10.1016/j.watres.2018.02.066.
2. Pereira, A.; Silva, L.; Laranjeiro, C.; Lino, C.; Pena, A. Selected Pharmaceuticals in Different Aquatic Compartments: Part I—Source, Fate and Occurrence. *Molecules* **2020**, *25*, 1026, doi:10.3390/molecules25051026.
3. Kucharski, D.; Nałęcz-Jawecki, G.; Drzewicz, P.; Skowronek, A.; Mianowicz, K.; Strzelecka, A.; Giebułtowicz, J. The Assessment of Environmental Risk Related to the Occurrence of Pharmaceuticals in Bottom Sediments of the Odra River Estuary (SW Baltic Sea). *Sci. Total Environ.* **2022**, *828*, 154446, doi:10.1016/j.scitotenv.2022.154446.
4. Liu, Q.; Feng, X.; Chen, N.; Shen, F.; Zhang, H.; Wang, S.; Sheng, Z.; Li, J. Occurrence and Risk Assessment of Typical PPCPs and Biodegradation Pathway of Ribavirin in Wastewater Treatment Plants. *Environ. Sci. Ecotechnology* **2022**, *11*, 100184, doi:10.1016/j.ese.2022.100184.
5. World Health Organization *Pharmaceuticals in Drinking-Water*; 2013;
6. Khan, S.; Naushad, M.; Govarthanan, M.; Iqbal, J.; Alfadul, S.M. Emerging Contaminants of High Concern for the Environment: Current Trends and Future Research. *Environ. Res.* **2022**, *207*, 112609, doi:10.1016/j.envres.2021.112609.
7. Houtman, C.J. Emerging Contaminants in Surface Waters and Their Relevance for the Production of Drinking Water in Europe. *J. Integr. Environ. Sci.* **2010**, *7*, 271–295, doi:10.1080/1943815X.2010.511648.
8. Benitez, F.J.; Acero, J.L.; Real, F.J.; Roldan, G.; Casas, F. Comparison of Different Chemical Oxidation Treatments for the Removal of Selected Pharmaceuticals in Water Matrices. *Chem. Eng. J.* **2011**, *168*, 1149–1156, doi:10.1016/j.cej.2011.02.001.
9. Belet, A.; Wolfs, C.; Mahy, J.; Poelman, D.; Vreuls, C.; Gillard, N.; Lambert, S. Sol-Gel Syntheses of Photocatalysts for the Removal of Pharmaceutical Products in Water. *Nanomaterials* **2019**, *9*, 126, doi:10.3390/nano9010126.
10. Feng, Y.; Li, L.; Ge, M.; Guo, C.; Wang, J.; Liu, L. Improved Catalytic Capability of Mesoporous TiO₂ Microspheres and Photodecomposition of Toluene. *ACS Appl. Mater. Interfaces* **2010**, *2*, 3134–3140, doi:10.1021/am100620f.
11. Araña, J.; Herrera Melián, J.A.; Doña Rodríguez, J.M.; González Díaz, O.; Viera, A.; Pérez Peña, J.; Marrero Sosa, P.M.; Espino Jiménez, V. TiO₂-Photocatalysis as a Tertiary Treatment of Naturally Treated Wastewater. *Catal. Today* **2002**, *76*, 279–289, doi:10.1016/S0920-5861(02)00226-2.
12. Levinson, R.; Berdahl, P.; Akbari, H. Solar Spectral Optical Properties of Pigments—Part I: Model for Deriving Scattering and Absorption Coefficients from Transmittance and Reflectance Measurements. *Sol. Energy Mater. Sol. Cells* **2005**, *89*, 319–349, doi:10.1016/j.solmat.2004.11.012.
13. Zu, M.; Zhou, X.; Zhang, S.; Qian, S.; Li, D.-S.; Liu, X.; Zhang, S. Sustainable Engineering of TiO₂-Based Advanced Oxidation Technologies: From Photocatalyst to Application Devices. *J. Mater. Sci. Technol.* **2021**, *78*, 202–222, doi:10.1016/j.jmst.2020.10.061.
14. Youssef, Z.; Colombeau, L.; Yesmurzayeva, N.; Baros, F.; Vanderesse, R.; Hamieh, T.; Toufaily, J.; Frochot, C.; Roques-Carnes, T.; Acherar, S. Dye-Sensitized Nanoparticles for Heterogeneous Photocatalysis: Cases Studies with TiO₂, ZnO, Fullerene and Graphene for Water Purification. *Dyes Pigments* **2018**, *159*, 49–71, doi:10.1016/j.dyepig.2018.06.002.
15. Shayegan, Z.; Lee, C.-S.; Haghghat, F. TiO₂ Photocatalyst for Removal of Volatile Organic Compounds in Gas Phase – A Review. *Chem. Eng. J.* **2018**, *334*, 2408–2439, doi:10.1016/j.cej.2017.09.153.
16. Krakowiak, R.; Musial, J.; Bakun, P.; Spychała, M.; Czarczynska-Goslinska, B.; Mlynarczyk, D.T.; Koczorowski, T.; Sobotta, L.; Stanisiz, B.; Goslinski, T. Titanium Dioxide-Based Photocatalysts for Degradation of Emerging Contaminants Including Pharmaceutical Pollutants. *Appl. Sci.* **2021**, *11*, 8674, doi:10.3390/app11188674.
17. Pereira, G.F.M.; Tasso, T.T. From Cuvette to Cells: How the Central Metal Ion Modulates the Properties of Phthalocyanines and Porphyrazines as Photosensitizers. *Inorganica Chim. Acta* **2021**, *519*, 120271, doi:10.1016/j.ica.2021.120271.
18. Jang, B.U.; Choi, J.H.; Lee, S.J.; Lee, S.G. Synthesis and Characterization of Cu -Phthalocyanine Hybrid TiO₂ Sol. *J. Porphy. Phthalocyanines* **2009**, *13*, 779–786, doi:10.1142/S1088424609001054.
19. Rodríguez-Morgade, M.S.; Stuzhin, P.A. The Chemistry of Porphyrazines: An Overview. *J. Porphy. Phthalocyanines* **2004**, *08*, 1129–1165, doi:10.1142/S1088424604000490.
20. de la Torre, G.; Claessens, C.G.; Torres, T. Phthalocyanines: Old Dyes, New Materials. Putting Color in Nanotechnology. *Chem Commun* **2007**, 2000–2015, doi:10.1039/B614234F.
21. Vignesh, K.; Rajarajan, M.; Suganthi, A. Photocatalytic Degradation of Erythromycin under Visible Light by Zinc Phthalocyanine-Modified Titania Nanoparticles. *Mater. Sci. Semicond. Process.* **2014**, *23*, 98–103, doi:10.1016/j.mssp.2014.02.050.
22. Mapukata, S.; Nyokong, T. Development of Phthalocyanine Functionalised TiO₂ and ZnO Nanofibers for Photodegradation of Methyl Orange. *New J. Chem.* **2020**, *44*, 16340–16350, doi:10.1039/D0NJ03326J.

23. Fei, J.; Han, Z.; Deng, Y.; Wang, T.; Zhao, J.; Wang, C.; Zhao, X. Enhanced Photocatalytic Performance of Iron Phthalocyanine/TiO₂ Heterostructure at Joint Fibrous Interfaces. *Colloids Surf. Physicochem. Eng. Asp.* **2021**, *625*, 126901, doi:10.1016/j.colsurfa.2021.126901.
24. Colbea, C.; Oancea, P.; Puiu, M.; Galaon, T.; Raducan, A. Reusable Hybrid Nanocomposites for Clean Degradation of Dye Waste under Visible Light. *Mater. Today Commun.* **2022**, *30*, 103091, doi:10.1016/j.mtcomm.2021.103091.
25. Szymczak, J.; Kryjewski, M. Porphyrins and Phthalocyanines on Solid-State Mesoporous Matrices as Catalysts in Oxidation Reactions. *Materials* **2022**, *15*, 2532, doi:10.3390/ma15072532.
26. Musial, J.; Krakowiak, R.; Frankowski, R.; Spychala, M.; Dlugaszewska, J.; Dobosz, B.; Bendzinska-Berus, W.; Krzyminiowski, R.; Tykarska, E.; Zgoła-Grześkowiak, A.; et al. Simple Modification of Titanium(IV) Oxide for the Preparation of a Reusable Photocatalyst. *Mater. Sci. Eng. B* **2022**, *276*, 115559, doi:10.1016/j.mseb.2021.115559.
27. Krakowiak, R.; Musial, J.; Frankowski, R.; Spychala, M.; Mielcarek, J.; Dobosz, B.; Krzyminiowski, R.; Sikorski, M.; Bendzinska-Berus, W.; Tykarska, E.; et al. Phthalocyanine-Grafted Titania Nanoparticles for Photodegradation of Ibuprofen. *Catalysts* **2020**, *10*, 1328, doi:10.3390/catal10111328.
28. Zhang, L.; Cole, J.M. Anchoring Groups for Dye-Sensitized Solar Cells. *ACS Appl. Mater. Interfaces* **2015**, *7*, 3427–3455, doi:10.1021/am507334m.
29. Genc, E.; Yüzer, A.C.; Yanalak, G.; Harputlu, E.; Aslan, E.; Ocakoglu, K.; Ince, M.; Patir, I.H. The Effect of Central Metal in Phthalocyanine for Photocatalytic Hydrogen Evolution via Artificial Photosynthesis. *Renew. Energy* **2020**, *162*, 1340–1346, doi:10.1016/j.renene.2020.08.063.
30. Ramirez, C.; Antonacci, C.; Ferreira, J.; Sheardy, R.D. The Facile Synthesis and Characterization of Novel Cationic Metallated and Nonmetallated Tetrapyrroline Porphyrins Having Different Metal Centers. *Synth. Commun.* **2004**, *34*, 3373–3379, doi:10.1081/SCC-200030591.
31. Szulbinski, W.S.; Kincaid, J.R. Synthesis and Spectroscopic Characterization of Zinc Tetra(3,4-Pyridine)Porphyrin Entrapped within the Supercages of Y-Zeolite. *Inorg. Chem.* **1998**, *37*, 5014–5020, doi:10.1021/ic971118s.
32. Feofanov, A.; Grichine, A.; Karmakova, T.; Kazachkina, N.; Pecherskih, E.; Yakubovskaya, R.; Lukyanets, E.; Derkacheva, V.; Egret-Charlier, M.; Vigny, P. Chelation with Metal Is Not Essential for Antitumor Photodynamic Activity of Sulfonated Phthalocyanines. *Photochem. Photobiol.* **2007**, *75*, 527–533, doi:10.1562/0031-8655(2002)0750527CWMINE2.0.CO2.
33. Kubelka, P. New Contributions to the Optics of Intensely Light-Scattering Materials Part I. *J. Opt. Soc. Am.* **1948**, *38*, 448, doi:10.1364/JOSA.38.000448.
34. Tauc, J. Optical Properties of Amorphous Semiconductors. In *Amorphous and Liquid Semiconductors*; Tauc, J., Ed.; Springer US: Boston, MA, 1974; pp. 159–220 ISBN 978-1-4615-8705-7.
35. Jin, K.; Qin, M.; Li, X.; Wang, R.; Zhao, Y.; Wang, H. Z-Scheme Au@TiO₂/Bi₂WO₆ Heterojunction as Efficient Visible-Light Photocatalyst for Degradation of Antibiotics. *J. Mol. Liq.* **2022**, *364*, 120017, doi:10.1016/j.molliq.2022.120017.
36. Noroozi, R.; Gholami, M.; Farzadkia, M.; Rezaei Kalantary, R. Synthesis of New Hybrid Composite Based on TiO₂ for Photocatalytic Degradation of Sulfamethoxazole and Pharmaceutical Wastewater, Optimization, Performance, and Reaction Mechanism Studies. *Environ. Sci. Pollut. Res.* **2022**, *29*, 56403–56418, doi:10.1007/s11356-022-19375-9.
37. Bui, V.H.; Vu, T.K.; To, H.T.; Negishi, N. Application of TiO₂-Ceramic/UVA Photocatalyst for the Photodegradation of Sulfamethoxazole. *Sustain. Chem. Pharm.* **2022**, *26*, 100617, doi:10.1016/j.scp.2022.100617.
38. Zhang, J.; Zhou, P.; Liu, J.; Yu, J. New Understanding of the Difference of Photocatalytic Activity among Anatase, Rutile and Brookite TiO₂. *Phys Chem Chem Phys* **2014**, *16*, 20382–20386, doi:10.1039/C4CP02201G.
39. Cui, Z.-H.; Wu, F.; Jiang, H. First-Principles Study of Relative Stability of Rutile and Anatase TiO₂ Using the Random Phase Approximation. *Phys. Chem. Chem. Phys.* **2016**, *18*, 29914–29922, doi:10.1039/C6CP04973G.
40. Greenstein, K.E.; Nagorzanski, M.R.; Kelsay, B.; Verdugo, E.M.; Myung, N.V.; Parkin, G.F.; Cwiertny, D.M. Carbon–Titanium Dioxide (C/TiO₂) Nanofiber Composites for Chemical Oxidation of Emerging Organic Contaminants in Reactive Filtration Applications. *Environ. Sci. Nano* **2021**, *8*, 711–722, doi:10.1039/D0EN00975J.
41. Hurum, D.C.; Agrios, A.G.; Gray, K.A.; Rajh, T.; Thurnauer, M.C. Explaining the Enhanced Photocatalytic Activity of Degussa P25 Mixed-Phase TiO₂ Using EPR. *J. Phys. Chem. B* **2003**, *107*, 4545–4549, doi:10.1021/jp0273934.
42. Scanlon, D.O.; Dunnill, C.W.; Buckeridge, J.; Shevlin, S.A.; Logsdail, A.J.; Woodley, S.M.; Catlow, C.R.A.; Powell, Michael.J.; Palgrave, R.G.; Parkin, I.P.; et al. Band Alignment of Rutile and Anatase TiO₂. *Nat. Mater.* **2013**, *12*, 798–801, doi:10.1038/nmat3697.
43. Kosmulski, M. The Significance of the Difference in the Point of Zero Charge between Rutile and Anatase. *Adv. Colloid Interface Sci.* **2002**, *99*, 255–264, doi:10.1016/S0001-8686(02)00080-5.
44. Blakemore, J.D.; Hull, J.F.; Crabtree, R.H.; Brudvig, G.W. Aqueous Speciation and Electrochemical Properties of a Water-Soluble Manganese Phthalocyanine Complex. *Dalton Trans. Camb. Engl.* **2003**, *2003*, 7681–7688, doi:10.1039/c2dt30371j.
45. De, S.; Devic, T.; Fateeva, A. Porphyrin and Phthalocyanine-Based Metal Organic Frameworks beyond Metal-Carboxylates. *Dalton Trans.* **2021**, *50*, 1166–1188, doi:10.1039/D0DT03903A.
46. Wang, Z.; Mao, W.; Chen, H.; Zhang, F.; Fan, X.; Qian, G. Copper(II) Phthalocyanine Tetrasulfonate Sensitized Nanocrystalline Titania Photocatalyst: Synthesis in Situ and Photocatalysis under Visible Light. *Catal. Commun.* **2006**, *7*, 518–522, doi:10.1016/j.catcom.2006.01.010.

47. Zhou, S.; Lai, J.; Liu, X.; Huang, G.; You, G.; Xu, Q.; Yin, D. Selective Conversion of Biomass-Derived Furfuryl Alcohol into n-Butyl Levulinate over Sulfonic Acid Functionalized TiO₂ Nanotubes. *Green Energy Environ.* **2022**, *7*, 257–265, doi:10.1016/j.gee.2020.09.009.
48. Ji, T.; Li, Z.; Liu, C.; Lu, X.; Li, L.; Zhu, J. Niobium-Doped TiO₂ Solid Acid Catalysts: Strengthened Interfacial Polarization, Amplified Microwave Heating and Enhanced Energy Efficiency of Hydroxymethylfurfural Production. *Appl. Catal. B Environ.* **2019**, *243*, 741–749, doi:10.1016/j.apcatb.2018.11.013.
49. Zhang, L.; Cole, J.M.; Dai, C. Variation in Optoelectronic Properties of Azo Dye-Sensitized TiO₂ Semiconductor Interfaces with Different Adsorption Anchors: Carboxylate, Sulfonate, Hydroxyl and Pyridyl Groups. *ACS Appl. Mater. Interfaces* **2014**, *6*, 7535–7546, doi:10.1021/am502186k.
50. Oprea, C.I.; Panait, P.; Lungu, J.; Stamate, D.; Dumbravă, A.; Cimpoesu, F.; Gîrțu, M.A. DFT Study of Binding and Electron Transfer from a Metal-Free Dye with Carboxyl, Hydroxyl, and Sulfonic Anchors to a Titanium Dioxide Nanocluster. *Int. J. Photoenergy* **2013**, *2013*, 1–15, doi:10.1155/2013/893850.
51. Harima, Y.; Fujita, T.; Kano, Y.; Imae, I.; Komaguchi, K.; Ooyama, Y.; Ohshita, J. Lewis-Acid Sites of TiO₂ Surface for Adsorption of Organic Dye Having Pyridyl Group as Anchoring Unit. *J. Phys. Chem. C* **2013**, *117*, 16364–16370, doi:10.1021/jp405835y.
52. Ooyama, Y.; Inoue, S.; Nagano, T.; Kushimoto, K.; Ohshita, J.; Imae, I.; Komaguchi, K.; Harima, Y. Dye-Sensitized Solar Cells Based On Donor-Acceptor π -Conjugated Fluorescent Dyes with a Pyridine Ring as an Electron-Withdrawing Anchoring Group. *Angew. Chem. Int. Ed.* **2011**, *50*, 7429–7433, doi:10.1002/anie.201102552.
53. Mohamed, M.M.; Bayoumy, W.A.; Khairy, M.; Mousa, M.A. Synthesis of Micro-Mesoporous TiO₂ Materials Assembled via Cationic Surfactants: Morphology, Thermal Stability and Surface Acidity Characteristics. *Microporous Mesoporous Mater.* **2007**, *103*, 174–183, doi:10.1016/j.micromeso.2007.01.052.
54. Bezrodna, T.; Puchkovska, G.; Shimanovska, V.; Chashechnikova, I.; Khalyavka, T.; Baran, J. Pyridine-TiO₂ Surface Interaction as a Probe for Surface Active Centers Analysis. *Appl. Surf. Sci.* **2003**, *214*, 222–231, doi:10.1016/S0169-4332(03)00346-5.
55. Zaki, M.I.; Hasan, M.A.; Al-Sagheer, F.A.; Pasupulety, L. In Situ FTIR Spectra of Pyridine Adsorbed on SiO₂-Al₂O₃, TiO₂, ZrO₂ and CeO₂: General Considerations for the Identification of Acid Sites on Surfaces of Finely Divided Metal Oxides. *Colloids Surf. Physicochem. Eng. Asp.* **2001**, *190*, 261–274, doi:10.1016/S0927-7757(01)00690-2.
56. Mathew, S.; Sebastian, A.; Kuttassery, F.; Takagi, S.; Tachibana, H.; Inoue, H. Acid-Base Equilibria of Axial Ligand and Peripheral Pyridyl Group with Stepwise Formation of Nine Species of Aluminum (III) Tera(4-Pyridyl) Porphyrin. *Inorganica Chim. Acta* **2021**, *526*, 120529, doi:10.1016/j.ica.2021.120529.
57. Gutz, I.G.R. CurTiPot – PH and Acid-Base Titration Curves: Analysis and Simulation Freeware (Version 4.3.1) 2021. Available online: http://www.iq.usp.br/gutz/Curtipot_.html (accessed on 02/05/2022).
58. Mesgari, Z.; Gharagozlou, M.; Khosravi, A.; Gharanjig, K. Spectrophotometric Studies of Visible Light Induced Photocatalytic Degradation of Methyl Orange Using Phthalocyanine-Modified Fe-Doped TiO₂ Nanocrystals. *Spectrochim. Acta. A. Mol. Biomol. Spectrosc.* **2012**, *92*, 148–153, doi:10.1016/j.saa.2012.02.055.
59. Vallejo, W.; Navarro, K.; Díaz-Urbe, C.; Schott, E.; Zarate, X.; Romero, E. Zn(II)-Tetracarboxy-Phthalocyanine-Sensitized TiO₂ Thin Films as Antimicrobial Agents under Visible Irradiation: A Combined DFT and Experimental Study. *ACS Omega* **2021**, *6*, 13637–13646, doi:10.1021/acsomega.1c00658.
60. Priyanka, K.P.; Sankararaman, S.; Balakrishna, K.M.; Varghese, T. Enhanced Visible Light Photocatalysis Using TiO₂/Phthalocyanine Nanocomposites for the Degradation of Selected Industrial Dyes. *J. Alloys Compd.* **2017**, *720*, 541–549, doi:10.1016/j.jallcom.2017.05.308.
61. Hudec, P.; Smiešková, A.; idek, Z.; Schneider, P.; Šolcová, O. Determination of Microporous Structure of Zeolites by T-Plot Method—State-of-the-Art. In *Studies in Surface Science and Catalysis*; Aiello, R., Giordano, G., Testa, F., Eds.; Impact of Zeolites and other Porous Materials on the new Technologies at the Beginning of the New Millennium; Elsevier, 2002; Vol. 142, pp. 1587–1594.
62. Thommes, M.; Kaneko, K.; Neimark, A.V.; Olivier, J.P.; Rodriguez-Reinoso, F.; Rouquerol, J.; Sing, K.S.W. Physisorption of Gases, with Special Reference to the Evaluation of Surface Area and Pore Size Distribution (IUPAC Technical Report). *Pure Appl. Chem.* **2015**, *87*, 1051–1069, doi:10.1515/pac-2014-1117.
63. Gommès, C.J.; Ravikovitch, P.; Neimark, A. Positive Curvature Effects and Interparticle Capillary Condensation during Nitrogen Adsorption in Particulate Porous Materials. *J. Colloid Interface Sci.* **2007**, *314*, 415–421, doi:10.1016/j.jcis.2007.05.072.
64. Wu, L.; Yu, J.C.; Zhang, L.; Wang, X.; Ho, W. Preparation of a Highly Active Nanocrystalline TiO₂ Photocatalyst from Titanium Oxo Cluster Precursor. *J. Solid State Chem.* **2004**, *177*, 2584–2590, doi:10.1016/j.jssc.2004.03.033.
65. Islam, S. Fast Responsive Anatase Nanoparticles Coated Fiber Optic PH Sensor. *J. Alloys Compd.* **2021**, *850*, 156246, doi:10.1016/j.jallcom.2020.156246.
66. Cadman, C.J.; Pucci, A.; Cellesi, F.; Tirelli, N. Water-Dispersible, Ligand-Free, and Extra-Small (<10 Nm) Titania Nanoparticles: Control Over Primary, Secondary, and Tertiary Agglomeration Through a Modified “Non-Aqueous” Route. *Adv. Funct. Mater.* **2014**, *24*, 993–1003, doi:10.1002/adfm.201301998.
67. Li, D.; Zhang, P.; Ge, S.; Sun, G.; He, Q.; Fa, W.; Li, Y.; Ma, J. A Green Route to Prepare Metal-Free Phthalocyanine Crystals with Controllable Structures by a Simple Solvothermal Method. *RSC Adv.* **2021**, *11*, 31226–31234, doi:10.1039/D1RA04064B.
68. Pająk, A.; Rybiński, P.; Janowska, G.; Kucharska-Jastrzabek, A. The Thermal Properties and the Flammability of Pigmented Elastomeric Materials. *J. Therm. Anal. Calorim.* **2014**, *117*, 789–798, doi:10.1007/s10973-014-3739-x.

69. Rodríguez-Mozaz, S.; Chamorro, S.; Marti, E.; Huerta, B.; Gros, M.; Sánchez-Melsió, A.; Borrego, C.M.; Barceló, D.; Balcázar, J.L. Occurrence of Antibiotics and Antibiotic Resistance Genes in Hospital and Urban Wastewaters and Their Impact on the Receiving River. *Water Res.* **2015**, *69*, 234–242, doi:10.1016/j.watres.2014.11.021.
70. Chang, H.; Hu, J.; Asami, M.; Kunikane, S. Simultaneous Analysis of 16 Sulfonamide and Trimethoprim Antibiotics in Environmental Waters by Liquid Chromatography–Electrospray Tandem Mass Spectrometry. *J. Chromatogr. A* **2008**, *1190*, 390–393, doi:10.1016/j.chroma.2008.03.057.
71. Göbel, A.; McArdell, C.S.; Suter, M.J.-F.; Giger, W. Trace Determination of Macrolide and Sulfonamide Antimicrobials, a Human Sulfonamide Metabolite, and Trimethoprim in Wastewater Using Liquid Chromatography Coupled to Electrospray Tandem Mass Spectrometry. *Anal. Chem.* **2004**, *76*, 4756–4764, doi:10.1021/ac0496603.
72. Dąbrowski, J.M.; Pucelik, B.; Regiel-Futyra, A.; Brindell, M.; Mazuryk, O.; Kyzioł, A.; Stochel, G.; Macyk, W.; Arnaut, L.G. Engineering of Relevant Photodynamic Processes through Structural Modifications of Metallotetrapyrrolic Photosensitizers. *Coord. Chem. Rev.* **2016**, *325*, 67–101, doi:10.1016/j.ccr.2016.06.007.
73. Miller, J.S.; Cornwell, D.G. The Role of Cryoprotective Agents as Hydroxyl Radical Scavengers. *Cryobiology* **1978**, *15*, 585–588, doi:10.1016/0011-2240(78)90082-2.
74. Misik, V.; Riesz, P. Free Radical Formation by Ultrasound in Organic Liquids: A Spin Trapping and EPR Study. *J. Phys. Chem.* **1994**, *98*, 1634–1640, doi:10.1021/j100057a016.
75. Gupta, S.; Goma, H.; Ray, M.B. A Novel Submerged Photocatalytic Oscillatory Membrane Reactor for Water Polishing. *J. Environ. Chem. Eng.* **2021**, *9*, 105562, doi:10.1016/j.jece.2021.105562.
76. European Chemicals Agency Titanium Dioxide - Brief Profile 2022. Available online: <https://echa.europa.eu/brief-profile/-/briefprofile/100.033.327> (accessed on 20/04/2022).